CCDC32 stabilizes clathrin-coated pits and drives their invagination

Ziyan Yang[1], Changsong Yang[2], Peiliu Xu[1], Lu Han[1], Yueping Li[1], Linyuan Peng[1], Xiangying Wei[3], Sandra L. Schmid[4,5], Tatyana Svitkina[2], Zhiming Chen[1,*]

[1] NHC Key Laboratory of Birth Defect Research and Prevention, MOE Key Laboratory of Rare Pediatric Diseases, Institute of Cytology and Genetics of School of Basic Medical Sciences & Department of Clinical Laboratory of The First Affiliated Hospital, Hengyang Medical School, University of South China, Hengyang, Hunan, China. [2] Department of Biology, University of Pennsylvania, Philadelphia, PA, USA. [3] Fuzhou Institute of Oceanography, College of Geography and Oceanography, Minjiang University, Fuzhou, Fujian, China. [4] Department of Cell Biology, University of Texas Southwestern Medical Center, Dallas, Texas, USA. [5] current address: Chan Zuckerberg Biohub, San Francisco, California, USA.

*To whom correspondence may be addressed. Email: Zhiming.Chen@usc.edu.cn

Author Contributions: Z. Chen, Z. Yang, and C. Yang designed the experiments. Z. Chen, Z. Yang, C. Yang, T. Svitkina and S.L. Schmid interpreted the results and wrote the manuscript with input from all authors. Z. Yang and Y. Li performed the TIRF and Epi-TIRF microscope imaging and data analysis. Z. Yang performed the co-IP, GST pull-down assays and TfnR uptake assays. C. Yang performed the PREM experiments. P. Xu performed FACS sorting. L. Han drew the cartoon illustrations.

Competing Interest Statement

The authors declare no competing interests.

Classification

Biological Sciences: Cell biology.

Key Words: endocytosis, clathrin, CCDC32, AP2, CFNDS

Abstract

Clathrin-mediated endocytosis (CME) is essential for maintaining cellular homeostasis. Previous studies have reported more than 50 CME accessory proteins; however, the mechanism driving the invagination of clathrin-coated pits (CCPs) remains elusive. Quantitative live cell imaging reveals that CCDC32, a poorly characterized endocytic accessory protein, regulates CCP stabilization and is required for efficient CCP invagination. CCDC32 interacts with the α-appendage domain (AD) of AP2 via its coiled-coil domain to exert this function. Furthermore, we showed that the clinically observed nonsense mutations in CCDC32, which result in the development of cardio-facio-neuro-developmental syndrome (CFNDS), inhibit CME by abolishing CCDC32-AP2 interactions. Overall, our data demonstrates the function and molecular mechanism of a novel endocytic accessory protein, CCDC32, in CME regulation.

Significance Statement

Clathrin-mediated endocytosis (CME) happens via the initiation, stabilization, and invagination of clathrin-coated pits (CCPs). In this study, we used a combination of quantitative live cell imaging, ultrastructure electron microscopy and biochemical experiments to show that CCDC32, a poorly studied and functional ambiguous protein, acts as an important endocytic accessory protein that regulates CCP stabilization and invagination. Specifically, CCDC32 exerts this function via its interactions with AP2, and the coiled-coil domain of CCDC32 and the α-appendage domain (AD) of AP2 are essential in mediating CCDC32-AP2 interactions. Importantly, we demonstrate that clinically observed loss-of-function mutations in CCDC32 lose AP2 interaction capacity and inhibit CME, resulting in the development of cardio-facio-neuro-developmental syndrome (CFNDS).

Main Text

Clathrin-mediated endocytosis (CME) regulates nutrient uptake and maintains the activity of transmembrane transporters and is thus, essential for maintaining cellular homeostasis (1-5). Malfunctions of CME are strongly associated with neurological diseases, cardiovascular diseases, and cancers (6-13). CME occurs via the assembly of clathrin triskelia into clathrin-coated pits (CCPs) that invaginate to form clathrin-coated vesicles (CCVs) (1, 4, 14). During CCP maturation, successful invagination of the clathrin coat and its underlying membrane is a key step that determines whether nascent CCPs are productive or abortive (15-18). Although more than 50 endocytic accessory proteins (EAPs) have been reported to be involved in the progression of CME (2, 3, 16, 19-23), the mechanism of CCP invagination remains elusive, i.e. which accessory proteins are required and how do they regulate CCP invagination?

Coiled-coil domain-containing protein 32 (CCDC32, Fig. S1), also known as gene *C15orf57*, is a small, 185 amino acids (aa) protein that has been poorly studied and whose function is unknown. Clinical genome sequencing of three patients with cardio-facio-neuro-developmental syndrome (CFNDS) revealed three homozygous nonsense mutations that only express the first 9, 54 and 81aa of CCDC32, respectively (24, 25). How these loss-of-function mutations result in CFNDS remains unknown.

A recent genome-wide co-essential modules study (26) suggested a functional correlation between CCDC32 and AP2, whose interactions were also implied by previous affinity purification-mass spectroscopy (AP-MS) analysis (27) and co-immunoprecipitation (co-IP) assays (26). In addition, depletion of CCDC32 was observed to inhibit transferrin uptake, suggesting a role in CME (26). Nevertheless, how CCDC32 interacts with AP2 and what role it plays in regulating CME remains unknown. In this study, we used a combination of quantitative live cell imaging, ultrastructure electron microscopy and biochemical experiments to show that CCDC32 binds to the α-appendage domain (α-AD) of AP2 via its coiled-coil domain and plays an early role in CME by regulating the stabilization and invagination of CCPs. Moreover, clinically observed loss-of-function mutations in CCDC32 lose AP2 interaction capacity and inhibit CME.

Results

CCDC32 is recruited to CCPs

To determine whether CCDC32 directly regulates CME, we first tested if and when CCDC32 is recruited to CCPs. ARPE-HPV cells that stably express mRuby-clathrin light chain a (mRuby-CLCa) and siRNA-resistant eGFP-tagged full-length CCDC32 (eGFP-CCDC32(FL)) were generated and imaged using Total Internal Reflection Fluorescence Microscopy (TIRFM). After

siRNA-mediated knockdown of endogenous CCDC32 (Fig. S2), we observed colocalization of eGFP-CCDC32(FL) and mRuby-CLCa (Fig. 1A) at the plasma membrane (PM), which is consistent with the prior observation in HeLa cells (26).

Furthermore, cohort-averaged fluorescence intensity traces were obtained using time-lapse imaging and primary (mRuby-CLCa)/subordinate (eGFP-CCDC32) tracking powered by cmeAnalysis (17, 28, 29). Importantly, more than half of analyzed CCPs were observed to recruit CCDC32, and the recruitment curve of CCDC32 follows the assembly of clathrin on CCPs (Fig. 1B), indicating that CCDC32 is recruited early to CCPs and is positioned to play a direct role in regulating CME. As a negative control, ARPE-HPV cells that stably express mRuby-CLCa and eGFP showed no eGFP recruitment to CCPs (Fig. 1C,D).

CCDC32 depletion inhibits transferrin receptor (TfnR) uptake and CCP formation

To gain further insight into the function of CCDC32 in CME, we knocked down CCDC32 in ARPE-HPV cells and examined its effects on TfnR uptake. In agreement with the previous observation (26), CCDC32 knockdown reduced the cellular uptake efficiency of TfnR (Fig. 2A,B).

To further define which stages of CME are dependent on CCDC32, we knocked down CCDC32 in ARPE-HPV cells that stably express eGFP-CLCa and employed quantitative live-cell TIRFM to visualize and analyze CCP dynamics (30). The movies and kymographs of time-lapse imaging showed that CCDC32 depletion resulted in the formation of large (i.e. brighter), static clathrin-coated structures (CCSs) (Fig. 2C,D & Movies 1,2) that dominate the images. However, we also noted a subpopulation of dynamic CCPs (arrows, Fig. 2D) that were visually obscured by large static CCSs, yet represent the majority of total CCSs detected. Indeed, despite the deceptive images, the percentage of static CCSs was only 7.8%.

To quantify the dynamic behaviors of CCPs, we performed cmeAnalysis (17, 29, 31) and DASC (disassembly asymmetry score classification) (15), which together provide a comprehensive and unbiased characterization of CCP intermediates and CME progression when CCDC32 was depleted. DASC, which distinguishes abortive from productive CCPs, revealed an increased rate of initiation of clathrin-coated structures (CCSs) (Fig. 2E), but a reduced rate of *bona fide* CCP initiation (Fig. 2F) and lower percentage of stable, *bona fide* CCPs (CCP%) (Fig. 2G). Together these data reveal an early defect in the growth and stabilization of nascent clathrin assemblies to form *bona fide* CCPs (15). Consistent with this, the dynamic population of CCPs exhibited shorter lifetimes upon CCDC32 knockdown (Fig. 2H).

Together these results demonstrate that CCDC32 is an important endocytic accessory protein involved in CCP stabilization and maturation. Strikingly, despite the profound effects of

CCDC32 depletion on CCP dynamics, the efficiency of TfnR uptake was only marginally affected (Fig. 2B). These paradoxical effects are typical of endocytic accessory proteins and indicative of functional redundancy or the induction of compensatory mechanisms (15, 17, 22). Indeed, a similar phenotype was previously observed in cells expressing a truncated AP2 mutant lacking the α-AD (17), a binding site for multiple EAPs, reflecting the resilience and plasticity of CME.

CCDC32 regulates CCP invagination

During CCP maturation, successful invagination of the clathrin coat and its underlying membrane has been identified as a key step that determines the fate of CCPs (15, 17). To determine whether CCDC32 regulates CCP invagination, we first used Epifluorescence (Epi)-TIRF microscopy to measure CCP invagination in live cells (Fig. 3A). In this approach, time-lapse Epi and TIRF fluorescence signals were near-simultaneously acquired for ARPE-HPV eGFP-CLCa cells (Fig. 3B) and analyzed using primary (TIRF-channel)/subordinate (Epi-channel) tracking powered by cmeAnalysis (15). The resulting Epi and TIRF fluorescence intensity traces of CCPs with similar lifetimes were then aligned and averaged to yield intensity cohorts, which were further logarithmically transformed to give average traces of the invagination depth (Δz) of the CCPs' center-of-mass (Fig. 3A,C). Here, we chose to present the ~30s lifetime cohort because they represent the invagination behavior of the most frequent tracks (Fig. 2H). CCDC32 knockdown strongly inhibited CCP invagination (Fig. 3C), suggesting a key role for CCDC32 in regulating this critical early stage in CME.

To independently validate that CCDC32 regulates CCP invagination, we next used Platinum Replica Electron Microscopy (PREM)(32) to examine the clathrin-coated structures (CCSs) at higher resolution. Strikingly, CCDC32 knockdown resulted in a substantial increase in the number (Fig. 4A-C) and size (Fig. 4D) of flat (pseudo-colored blue) CCSs and a corresponding higher occupancy of CCSs on the PM (Fig. 4E; Fig. S3D), consistent with TIRFM and Epi-TIRF microscopy observations. Importantly, while significantly decreased in both number and size, dome-shaped (green) and spherical (orange) CCSs were still detected, likely corresponding to intermediates within the larger subpopulation of dynamic CCPs (Fig. 4A-D; Fig. S3A-C). The PREM results provide high resolution structural data, supporting a critical role for CCDC32 in regulating CCP invagination.

CCDC32 interacts with AP2 through the α-appendage domain

Next, we explored the mechanism behind CME regulation by CCDC32. The adaptor AP2, which is essential for CCP and CCV formation, is a heterotetramer consisting of α, β, μ, and σ subunits

(Fig. 5A). A previous study reported interactions between CCDC32 and AP2 (26), but the binding sites were not identified. To first validate that CCDC32 interacts with AP2, we conducted co-immunoprecipitation (co-IP) from cell lysate of ARPE-HPV cells that stably express eGFP-tagged α-subunit of AP2 (AP2-α-eGFP, Fig. 5B) (33). Mass Spectrometry analysis revealed, as expected, the co-IP of well-known AP2 binding proteins (i.e. EPS15, NECAP2, AAK1 and AAGAB)(1). Notably, CCDC32 was also efficiently co-immunoprecipitated with AP2 (Fig. 5C; Table S1).

Most endocytic accessory proteins interact with AP2 via the appendage domains of the α and β subunits (34, 35) (Fig. 5A, α-AD and β-AD). Therefore, we expressed and purified GST-tagged AP2 α-AD and β-AD (Fig. 5D) and used GST pull-down assays to test which might interact with CCDC32. GST-AP2-α-AD, but not GST-AP2-β-AD, was capable of pulling down CCDC32 from ARPE-HPV eGFP-CCDC32(FL) cell lysate (Fig. 5E,F). Thus, CCDC32 interacts with AP2 via the α-AD. Furthermore, we observed that co-IP of eGFP-CCDC32(FL) efficiently precipitated AP2 from ARPE-HPV cell lysate, while co-IP of eGFP did not (Fig. 5G-I).

The coiled-coil domain of CCDC32 mediates CCDC32-AP2 interactions

We next identified the region on CCDC32 responsible for AP2 binding, focusing first on the coiled-coil domain, which are known to facilitate protein-protein interactions (36), located in the middle of CCDC32. Thus, we engineered an siRNA-resistant eGFP-CCDC32 construct lacking the coiled-coil domain (Δ78-98, Fig. 6A; Fig. S1), and stably expressed it in ARPE-HPV cells with comparable expression level with eGFP-CCDC32(FL) (Fig. S2A). While AP2 efficiently co-IPs with full length CCDC32 from cell lysates, little AP2 above background co-IPs with CCDC32(Δ78-98) (Fig. 6B,C). Thus, the coiled-coil domain of CCDC32 is essential for CCDC32-AP2 interactions. Consistent with this, no obvious recruitment of CCDC32(Δ78-98) to CCPs was observed (Fig. 6D,E), indicating that CCDC32 is likely recruited to CCPs through its interactions with AP2. Notably, CCDC32(Δ78-98) was unable to rescue either the uptake of the CME cargo, TfnR (Fig. 6F) or the stabilization of CCPs (Fig. 6G).

Together, these results establish that CCDC32, a previously uncharacterized endocytic accessory protein, is recruited to CCPs via interactions between its coiled-coil domain and the α-AD of AP2, where it plays a critical role in regulating CCP stabilization and invagination.

Disease-causing nonsense mutation in CCDC32 loses AP2 interaction capacity and inhibits CME

Loss-of-function nonsense mutations in CCDC32 have been reported to result in CFNDS (24, 25); however, the disease-causing mechanism remains unknown. The identified frameshift mutations

result in premature termination and truncation of the protein at residue 10, 54 or 81 (24). Based on our findings, we hypothesize that these C-terminally truncated mutants will be defective in AP2 binding and unable to function in CME. To test this hypothesis, we generated an siRNA-resistant eGFP-CCDC32(1-54) construct (Fig. 7A) based on the clinical report (24), and stably expressed this truncated CCDC32 mutant in ARPE-HPV cells (Fig. S2A).

As predicted, AP2 did not co-IP with CCDC32(1-54) from the cell lysate (Fig. 7B,C), confirming that the disease-causing mutation in CCDC32 abolishes its interactions with AP2. Correspondingly, we could not detect CCDC32(1-54) recruitment to CCPs in dual channel TIRFM imaging (Fig. 7D,E), consistent with CCP recruitment of CCDC32 being dependent on CCDC32-AP2 interactions. Finally, we observed that expression of eGFP-CCDC32(1-54), after siRNA-mediated knockdown of endogenous CCDC32, was unable to rescue TfnR uptake efficiency (Fig. 7F, Fig. S2B) or CCP stabilization (Fig. 7G). These findings show that loss-of-function nonsense mutation in CCDC32 abolishes its interactions with AP2, and thus inhibits CME, resulting in the development of CFNDS.

Discussion

CCDC32 was identified through genetic studies, originally in a yeast 2-hybrid screen for proteins interacting with annexin A2 (37) and subsequently via whole exome sequencing to identify mutations associated with cranio-facio-neurodevelopmental syndrome (CFNDS) (24, 25). More recently, bioinformatic analysis of co-essential modules linked CCDC32 with the AP2 adaptor complex, confirmed its interaction with AP2 and demonstrated a role in CME (26). Here we characterize the CCDC32-AP2 interaction, which we show is required for its recruitment to CCPs. Our data demonstrate that CCDC32 plays a critical role at early stages of CME. Depletion of CCDC32 results in a pronounced defect in CCP invagination, a decrease in the rate of formation and percentage of stabilized nascent CCPs and an accumulation of large flat clathrin lattices (Fig. 8). Despite these profound alterations in CCP dynamics, CME itself, as measured by TfnR internalization efficiencies, is only partially inhibited. We speculate that this mild endocytic defect reflects the plasticity and resilience of CME. Indeed, we detect two potential compensatory mechanisms that occur upon depletion of CCDC32, namely an increase in the rate of CCS assembly and a decrease in the lifetimes of dynamic CCPs (i.e. an increased rate of CCP maturation) (Fig. 8).

While depletion of other endocytic accessory proteins has been reported to result in one or more of these phenotypes, to our knowledge, this combination of phenotypes has not been detected. Instead, either CCP assembly is reduced (38, 39) or CCPs accumulate at later stages

of invagination (3, 40). These phenotypes have, however, been observed previously in cells expressing a truncated mutant of AP2 lacking the α-AD (17). These cells also showed near normal Tfn uptake, but accumulated flat clathrin lattices, showed an increase in the rate of nascent CCS initiation, impaired stabilization of dynamic CCPs and a decrease in CCP lifetimes. We speculate that loss of CCDC32 recruitment could have accounted for these unique phenotypes.

Although the mechanism of CCP invagination has been an important topic for decades, which endocytic accessory proteins (if any) regulate CCP invagination and (if so) how, has remained unclear. The depletion of CCDC32 in cells strongly inhibited the formation of dome-shaped and spherical CCSs, and instead resulted in the accumulation of large flat CCSs. This experimentally observed requirement of CCDC32 in CCP invagination is consistent with previous findings that clathrin assembly alone was not sufficient to induce CCP invagination in cells (17), potentially due to the reported flexibility of clathrin coats (41, 42). The mechanism by which CCDC32 promotes CCP invagination remains to be determined, but other domains of the protein may bind to and stabilize the clathrin coat, or the predicted largely disordered structure of CCDC32 (Fig. S1) may generate membrane curvature by molecular crowding (43).

We localized the α-AD binding site on CCDC32 to a short, predicted alpha-helical region (aa78-98). Interestingly, this sequence, LASLEKKLRRIKGLNQEVTSKD, does not encode any of the known AP2 α-AD binding motifs (e.g. DxF/W, FxDxF, WxxF/W, FxxFxxL) commonly shared amongst other AP2 interacting partners(44). Thus, we speculate that CCDC32 might bind at a discrete site on the α-AD perhaps uniquely positioning it for interactions with the clathrin coat and/or membrane.

Our results provide a compelling mechanistic explanation for how the clinically observed loss-of-function mutations in CCDC32 result in the development of CFNDS. The disease-associated CCDC32 loss-of-function mutants are not capable of interacting with AP2, thus losing their AP2 regulation capacity. The resulting dysregulation of AP2 inhibits CME, which further results in the development of CFNDS. Importantly, the clinical features of CCDC32 loss-of-function are similar to those resulting from AP2 loss-of-function(45-50), supporting that CCDC32 functions through AP2.

In summary, our study identified CCDC32 as an important endocytic accessory protein that regulates CCP stabilization and invagination via its interactions with AP2. Future work needs to address exactly how CCDC32 enhances curvature generation and coat stabilization. A structural biological study to reveal more details of CCDC32-AP2 interactions will also advance our understanding of CCDC32.

Materials and Methods

Plasmids

The eGFP-CCDC32(FL, human) fragment in a pEGFP-C1 vector was purchased from Addgene (#110505) and then mutated to be siRNA resistant, which retained amino acid sequence (#98-102) while modifying the nucleotide sequence. Next, aa78-98 was deleted from siRNA resistant eGFP-CCDC32(FL) to generate eGFP-CCDC32(Δ78-98). Finally, eGFP, eGFP-CCDC32(1-54), eGFP-CCDC32(Δ78-98), and eGFP-CCDC32(FL) were separately cloned into a pLVx-CMV100 vector (51) using NEBuilder® HiFi DNA Assembly Master Mix (Catalog #E2621). Primers used for mutagenesis and cloning are listed below:

Mutagenesis	**Forward primer**	**Reverse primer**
eGFP-CCDC32(Δ78-98)	*GCAGGATTCAGAAGTGTATGACATGCTTCGAACTCTG*	*CAGAGTTCGAAGCATGTCATACACTTCTGAATCCTGC*
siRNA Resistant of eGFP-CCDC32(FL)	*CAGGAAGTGACTTCCAAGGATATGTTACGCACCCTGGCCCAAGCCAAGAAGGA*	*TCCTTCTTGGCTTGGGCCAGGGTGCGTAACATATCCTTGGAAGTCACTTCCTG*
siRNA Resistant of eGFP-CCDC32(Δ78-98)	*TCCCTTGCAGGATTCAGAAGTGTATGATATGTTACGCACCCTGGCCCAAGCCAAGAA*	*TTCTTGGCTTGGGCCAGGGTGCGTAACATATCATACACTTCTGAATCCTGCAAGGGA*
Cloning	**Forward primer**	**Reverse primer**
backbone：pLVx-CMV100	*CGCCGCTAGCGCTAACTAGTATGGTGAGCAAGGGCGAG*	*GTCGGGCCCTCTAGACTCGAGTTACTGTTCTGCTGCTGCTG*
insert：eGFP-CCDC32(FL)		
backbone：pLVx-CMV100	*CGCCGCTAGCGCTAACTAGTATGGTGAGCAAGGGCGAG*	*CGGGCCCTCTAGACTCGAGTTACTTGTACAGCTCGTCCATGC*
insert：eGFP		
backbone：pLVx-CMV100	*CGCCGCTAGCGCTAACTAGTATGGTGAGCAAGGGCGAG*	*TCGGGCCCTCTAGACTCGAGCTACCTCTGGCCTTCACCTTC*
insert：eGFP-CCDC32(1-54)		
backbone：pLVx-CMV100	*CGCCGCTAGCGCTAACTAGTATGGTGAGCAAGGGCGAG*	*GTCGGGCCCTCTAGACTCGAGTTACTGTTCTGCTGCTGCTG*

insert：eGFP-CCDC32(Δ78-98)		

In addition, mRuby-CLCa in a pLVx-IRES-puro vector was generated in our previous study (52). AP2-α-AD (aa701-938, mouse) in a pGEX-2T-1 vector and AP2-β-AD (aa592-937, rat) in a pGEX-4T-1 vector were kind gifts of the late Linton Traub (University of Pittsburgh, PA).

Cell culture, lentivirus infection, siRNA transfection and rescue

ARPE-19 and ARPE19-HPV16 (herein called ARPE-HPV) cells were obtained from ATCC and cultured in DMEM/F12 (Gibco, Catalog #8122502) with 10% FBS. HEK293T cells were obtained from ATCC and cultured in DMEM (Gibco, Catalog #8122070) with 10% FBS. ARPE-HPV cells that stably express eGFP-CLCa were generated in our previous study (28).

Lentiviruses encoding mRuby-CLCa were produced in HEK293T packaging cells following standard transfection protocols (53) and harvested for subsequent infections to ARPE-HPV cells to generate ARPE-HPV mRuby-CLCa cells. Lentiviruses encoding siRNA-resistant eGFP, eGFP-CCDC32(1-54), eGFP-CCDC32(Δ78-98), and eGFP-CCDC32(FL) were produced in HEK293T packaging cells and harvested for subsequent infections to ARPE-HPV mRuby-CLCa cells. Infected cells were FACS sorted for homogenous mRuby and eGFP signals after 3 days and passaged for 2 weeks before experiments.

For siRNA-mediated knockdown of CCDC32, cells were seeded on 6-well plates (250,000 cells/well) and transfected with 2 rounds of siCCDC32 (Silencer Select Pre-designed siRNA ID#: s228444, targets aa98-102 sequence) through 3 days. Cells treated with siControl (Silencer Select Negative Control #1 siRNA, cat#:4390843) were used as negative control. Transfections of siRNA were mediated with Opti-MEM and Lipofectamine RNAi-MAX (Invitrogen) as detailed in ref(28).

For CCDC32 rescue experiments, siRNA-resistant eGFP, eGFP-CCDC32(1-54), eGFP-CCDC32(Δ78-98) and eGFP-CCDC32(FL) were homogenously expressed in ARPE-HPV mRuby-CLCa cells via lentiviral infection and FACS sorting, followed by siRNA-mediated knockdown of endogenous CCDC32. Anti-GFP Monoclonal Antibody (Proteintech, # 66002-1-Ig), Anti-Vinculin Polyclonal Antibody (Proteintech, #26520-1-AP), and anti-C15orf57 Polyclonal antibody (Invitrogen, #PA5-98982) were used in Western Blotting to confirm protein expression level and knockdown efficiency.

Co-immunoprecipitation (co-IP)

ARPE-HPV cells with stable expression of AP2-α-eGFP, eGFP, eGFP-CCDC32(1-54), eGFP-CCDC32(Δ78-98) or eGFP-CCDC32(FL) were cultured in a 15-cm dish. When confluence reached ~90%, cells were washed 3x with ice-cold PBS and detached with cell scratcher. Next, cells were spun down at 500 g, 4°C for 3 min, and then resuspended in 1ml ice-cold lysis buffer (50 mM Tris，pH 7.5，150 mM NaCl，1mM EDTA，0.5% Triton X-100，1× protease inhibitor，1mM PMSF). After 30 min rotation in a cold room and occasional vortexing, the lysed cells were spun at 500 g, 4°C, for 3 min to remove the nuclei. Subsequently, 50μl anti-GFP magnetic beads (Biolinkedin, #L1016) were added to cell lysate that contained 0.5mg proteins (determined by BCA assay). The reaction was allowed to proceed by rotation at 4°C for 2h and then precipitated with DynaMag. The sediments were washed with lysis buffer, and then resuspended and heat-denatured in 2x Laemmli buffer (supplemented with 5% β-Mercaptoethanol). The final samples were run into SDS-PAGE gels before: 1) being transferred to membranes for Western Blotting; or 2) being sent to the proteomics core facility for mass spectrometry analysis. Anti-α-Adaptin 1/2 Antibody (C-8) (Santa Cruz Biotechnology, Catalog #sc-17771) was used in WB to detect AP2 enrichments.

Protein purification and GST pull-down assay

GST in a pGEX-6P-1 vector, GST-AP2-α-AD in a pGEX-2T-1 vector, and GST-AP2-β-AD in a pGEX-4T-1 vector were transfected and expressed in BL21(DE3) separately, and then affinity purified using GSTrap HP column (Cytiva). The affinity-purified GST fusion proteins were applied to a HiLoad 16/600 Superdex 200 pg column (Cytiva). Target proteins were collected and concentrated using Amicon Ultra-15 10K Centrifugal filters (Sigma-Aldrich), and stored in 20 mM HEPES, 150 mM NaCl，1mM TCEP, pH 7.4.

In GST pull-down assays, purified GST, GST-AP2-α-AD, and GST-AP2-β-AD were pre-bound to anti-GST beads (Biolinkedin, #L-2004). Subsequently, these beads were separately added into 0.5 mg cell lysate of ARPE-HPV eGFP-CCDC32(FL). The reactions were allowed to proceed by rotation at 4°C for 2h, and then the beads were spun down at 1000 g, 4°C for 3 min. The sediments were washed with lysis buffer, and then heat-denatured in 2x Laemmli buffer (supplemented with 5% β-Mercaptoethanol) before running into SDS-PAGE gels, which followed by Western Blotting analysis.

Transferrin receptor (TfnR) uptake assay

Internalization of TfnR was quantified by in cell ELISA following established protocols described in refs (28, 52, 54). Briefly, ~15,000 cells were seeded on gelatin-coated 96-well plate overnight.

Next day, cells were starved in 37°C-warm PBS^{4+} (1× PBS buffer plus 0.2% BSA, 1mM $CaCl_2$, 1mM $MgCl_2$, and 5mM D-glucose) for 30 min. After starvation, the cell medium was replaced with ice-cold PBS^{4+} containing 5 μg/ml HTR-D65 (anti-TfnR mAb) (55). In parallel, some cells were kept at 4°C for the measurement of surface amount of TfnR (denoted as S) and blank controls (denoted as B), while some were incubated in a 37°C water bath for the indicated times for the measurement of internalized TfnR (denoted as I). For B and I, acid wash (0.2 M acetic acid and 0.2 M NaCl, pH 2.3) was applied to remove surface-bound HTR-D65. After washing with cold PBS. All cells were fixed with 4% PFA (Electron Microscopy Sciences) diluted in PBS for 30 min at 37°C. Subsequently, the cells were permeabilized with 0.1% Triton X-100 and blocked with Q-PBS (PBS, 2% BSA, 0.1% lysine, and 0.01% saponin, pH 7.4) for 2h. Surface-bound and internalized HTR-D65 were detected with HRP Goat anti-Mouse IgG (H+L) (BioRad) and o-phenylenediamine dihydrochloride (OPD, Sigma-Aldrich). Well-to-well variation of cell numbers was accounted for by BCA assays.

TIRF and Epi-TIRF microscopy

Cells for imaging were seeded on gelatin-coated glass bottom dishes 35 mm (ibidi, #81218-800) for ~12h before data acquisition. Live cell imaging was conducted with a Nikon Eclipse Ti2 inverted microscope that was equipped with: 1) an Apo TIRF/100x 1.49 Oil objective; 2) a Prime Back Illuminated sCMOS Camera (Prime BSI, 6.5 x 6.5μm pixel size and 95% peak quantum efficiency; 3) a M-TIRF module for epifluorescence (Epi) acquisition; 4) an H-TIRF module for TIRF acquisition, where penetration depth was fixed to 80nm; 5) an Okolab Cage Incubator for maintaining 37°C and 5% CO_2.

For time-lapse TIRF imaging, 451 consecutive images were acquired at a frame rate of 1 frame/s for single channel or 0.5 frame/s for dual channels. For time-lapse Epi-TIRF imaging, 451 consecutive Epi and TIRF images were acquired nearly simultaneously at a frame rate of 0.66 frame/s. Perfect Focus System (PFS) was applied during time-lapse imaging.

The acquired data was analyzed using cmeAnalysis (17, 29) and DASC (15), which are available at: https://github.com/DanuserLab/cmeAnalysis. Briefly, cmeAnalysis was used to track the lifetime and fluorescence of clathrin-coated structures, and then DASC was applied to unbiasedly classify *bona fide* CCPs vs. abortive coats. Next, the classified CCP tracks were used to calculate CCP invagination (Δz). Tracks that overlap with others or deviate from the properties of a diffraction-limited particle were excluded from the analysis.

Platinum Replica Electron Microscopy (PREM)

The “unroofing” technique that mechanically removes the upper cell plasma membrane while preserving the ventral plasma membrane with CCSs and other structures for PREM analyses was performed essentially as described previously (56). Briefly, ARPE19 cells treated with siCCDC32 or siControl on coverslips were quickly transferred into ice-cold PEM buffer (100 mM PIPES−KOH, pH 6.9, 1 mM MgCl2 and 1 mM EGTA) containing 2 μM unlabeled phalloidin (Sigma , #P2141) and 10 μM taxol (Sigma-Aldrich, #T7402) and unroofed by a brief (1s) ultrasonic burst from a 1/8-inch microprobe positioned at ~45° angle ~3 mm above the coverslip and operated by Misonix XL2020 Ultrasonic Processor at 17-20% of output power. After sonication, the coverslips were immediately fixed with 2% glutaraldehyde in 0.1 M Na-cacodylate buffer, pH 7.3 for at least 20 min at room temperature.

Sample processing for PREM was performed as described previously (57). In brief, glutaraldehyde-fixed cells were post-fixed by sequential treatment with 0.1% tannic acid and 0.2% uranyl acetate in water, critical-point dried, coated with platinum and carbon, and transferred onto EM grids for observation.

PREM samples were examined using JEM 1011 transmission electron microscope (JEOL USA, Peabody, MA) operated at 100 kV. Images were acquired by an ORIUS 832.10W CCD camera (Gatan, Warrendale, PA) and presented in inverted contrast.

Acknowledgements

We thank the UTSW proteomics core facility for their help with sample processing and analysis. We thank Justin Bi for PREM analysis. We thank Zhenyang Chen for active participation in protein preparation. This work is supported by the National Natural Science Foundation of China (Grant No. 32200564 to Z.C.), the Natural Science Foundation of Hunan Province, China (Grant No. 2024JJ2045), the National Institutes of Health grants R35 GM 140832 to T.S., and the National Institutes of Health grant GM73165 to S.L.S.

References

1. M. Mettlen, P. H. Chen, S. Srinivasan, G. Danuser, S. L. Schmid, Regulation of Clathrin-Mediated Endocytosis. *Annu Rev Biochem* **87**, 871-896 (2018).
2. T. Kirchhausen, D. Owen, S. C. Harrison, Molecular structure, function, and dynamics of clathrin-mediated membrane traffic. *Cold Spring Harb Perspect Biol* **6**, a016725 (2014).
3. H. T. McMahon, E. Boucrot, Molecular mechanism and physiological functions of clathrin-mediated endocytosis. *Nat Rev Mol Cell Biol* **12**, 517-533 (2011).
4. M. Kaksonen, A. Roux, Mechanisms of clathrin-mediated endocytosis. *Nature Reviews Molecular Cell Biology* **19**, 313-326 (2018).
5. S. M. Smith, C. J. Smith, Capturing the mechanics of clathrin-mediated endocytosis. *Curr Opin Struc Biol* **75** (2022).

6. F. Manti *et al.*, Neurotransmitter trafficking defect in a patient with clathrin (CLTC) variation presenting with intellectual disability and early-onset parkinsonism. *Parkinsonism & Related Disorders* **61**, 207-210 (2019).
7. F. F. Hamdan *et al.*, High Rate of Recurrent De Novo Mutations in Developmental and Epileptic Encephalopathies. *The American Journal of Human Genetics* **101**, 664-685 (2017).
8. J. DeMari *et al.*, CLTC as a clinically novel gene associated with multiple malformations and developmental delay. *American Journal of Medical Genetics Part A* **170**, 958-966 (2016).
9. F. Wu, P. J. Yao, Clathrin-mediated endocytosis and Alzheimer's disease: An update. *Ageing Res Rev* **8**, 147-149 (2009).
10. Ł. J. Sznajder, M. S. Swanson, Short Tandem Repeat Expansions and RNA-Mediated Pathogenesis in Myotonic Dystrophy. *International Journal of Molecular Sciences* **20**, 3365 (2019).
11. R. E. Blue, E. G. Curry, N. M. Engels, E. Y. Lee, J. Giudice, How alternative splicing affects membrane-trafficking dynamics. *Journal of Cell Science* **131**, jcs216465 (2018).
12. J. L. Gilles Moulay, Mégane Lemaître, Marc Bitoun, Denis Furling, Stéphane Vassilopoulos (2019) Revealing alternative splicing control of clathrin structural plasticity in health and disease. in *EMBO Conference Abstract*.
13. S. R. Elkin *et al.*, A Systematic Analysis Reveals Heterogeneous Changes in the Endocytic Activities of Cancer Cells. *Cancer Research* **75**, 4640-4650 (2015).
14. S. M. Smith, C. J. Smith, Capturing the mechanics of clathrin-mediated endocytosis. *Curr Opin Struc Biol* **75**, 102427 (2022).
15. X. Wang *et al.*, DASC, a sensitive classifier for measuring discrete early stages in clathrin-mediated endocytosis. *Elife* **9**, e53686 (2020).
16. Z. Chen, S. L. Schmid, Evolving models for assembling and shaping clathrin-coated pits. *Journal of Cell Biology* **219** (2020).
17. F. Aguet, Costin N. Antonescu, M. Mettlen, Sandra L. Schmid, G. Danuser, Advances in Analysis of Low Signal-to-Noise Images Link Dynamin and AP2 to the Functions of an Endocytic Checkpoint. *Developmental Cell* **26**, 279-291 (2013).
18. F. Baschieri, K. Porshneva, G. Montagnac, Frustrated clathrin-mediated endocytosis – causes and possible functions. *Journal of Cell Science* **133** (2020).
19. C. J. Merrifield, M. Kaksonen, Endocytic Accessory Factors and Regulation of Clathrin-Mediated Endocytosis. *Cold Spring Harbor Perspectives in Biology* **6** (2014).
20. K. A. Sochacki, A. M. Dickey, M.-P. Strub, J. W. Taraska, Endocytic proteins are partitioned at the edge of the clathrin lattice in mammalian cells. *Nature Cell Biology* **19**, 352-361 (2017).
21. M. J. Taylor, D. Perrais, C. J. Merrifield, A High Precision Survey of the Molecular Dynamics of Mammalian Clathrin-Mediated Endocytosis. *PLOS Biology* **9**, e1000604 (2011).
22. M. Bhave *et al.*, Functional characterization of 67 endocytic accessory proteins using multiparametric quantitative analysis of CCP dynamics. *Proc Natl Acad Sci U S A* **117**, 31591-31602 (2020).
23. L. M. Traub, Regarding the Amazing Choreography of Clathrin Coats. *Plos Biology* **9** (2011).
24. T. Harel *et al.*, Loss of function mutations in CCDC32 cause a congenital syndrome characterized by craniofacial, cardiac and neurodevelopmental anomalies. *Human Molecular Genetics* **29**, 1489-1497 (2020).
25. E. Abdalla, M. Alawi, P. Meinecke, K. Kutsche, F. L. Harms, Cardiofacioneurodevelopmental syndrome: Report of a novel patient and expansion of the phenotype. *Am J Med Genet A* **188**, 2448-2453 (2022).
26. M. Wainberg *et al.*, A genome-wide atlas of co-essential modules assigns function to uncharacterized genes. *Nature Genetics* **53**, 638-649 (2021).
27. E. L. Huttlin *et al.*, The BioPlex Network: A Systematic Exploration of the Human Interactome. *Cell* **162**, 425-440 (2015).

28. Z. Chen *et al.*, Wbox2: A clathrin terminal domain–derived peptide inhibitor of clathrin-mediated endocytosis. *Journal of Cell Biology* **219** (2020).
29. K. Jaqaman *et al.*, Robust single-particle tracking in live-cell time-lapse sequences. *Nat Methods* **5**, 695-702 (2008).
30. M. Mettlen, G. Danuser, Imaging and Modeling the Dynamics of Clathrin-Mediated Endocytosis. *Cold Spring Harbor Perspectives in Biology* **6** (2014).
31. D. Loerke, M. Mettlen, S. L. Schmid, G. Danuser, Measuring the Hierarchy of Molecular Events During Clathrin-Mediated Endocytosis. *Traffic* **12**, 815-825 (2011).
32. T. M. Svitkina, Platinum replica electron microscopy: Imaging the cytoskeleton globally and locally. *Int J Biochem Cell Biol* **86**, 37-41 (2017).
33. R. E. Mino, Z. Chen, M. Mettlen, S. L. Schmid, An internally eGFP-tagged α-adaptin is a fully functional and improved fiduciary marker for clathrin-coated pit dynamics. *Traffic* **21**, 603-616 (2020).
34. G. J. Praefcke *et al.*, Evolving nature of the AP2 alpha-appendage hub during clathrin-coated vesicle endocytosis. *EMBO J* **23**, 4371-4383 (2004).
35. E. M. Schmid *et al.*, Role of the AP2 β-Appendage Hub in Recruiting Partners for Clathrin-Coated Vesicle Assembly. *PLOS Biology* **4**, e262 (2006).
36. H. M. Strauss, S. Keller, "Pharmacological Interference with Protein-Protein Interactions Mediated by Coiled-Coil Motifs" in Protein-Protein Interactions as New Drug Targets, E. Klussmann, J. Scott, Eds. (Springer Berlin Heidelberg, Berlin, Heidelberg, 2008), 10.1007/978-3-540-72843-6_19, pp. 461-482.
37. Q. Li, Y. Laumonnier, T. Syrovets, T. Simmet, Yeast two-hybrid screening of proteins interacting with plasmin receptor subunit: C-terminal fragment of annexin A2. *Acta Pharmacol Sin* **32**, 1411-1418 (2011).
38. P. K. Umasankar *et al.*, A clathrin coat assembly role for the muniscin protein central linker revealed by TALEN-mediated gene editing. *Elife* **3** (2014).
39. W. M. Henne *et al.*, FCHo proteins are nucleators of clathrin-mediated endocytosis. *Science* **328**, 1281-1284 (2010).
40. M. Messa *et al.*, Epsin deficiency impairs endocytosis by stalling the actin-dependent invagination of endocytic clathrin-coated pits. *Elife* **3**, e03311 (2014).
41. M. L. Ferguson *et al.*, Clathrin triskelia show evidence of molecular flexibility. *Biophys J* **95**, 1945-1955 (2008).
42. G. Tagiltsev, C. A. Haselwandter, S. Scheuring, Nanodissected elastically loaded clathrin lattices relax to increased curvature. *Science Advances* **7** (2021).
43. D. J. Busch *et al.*, Intrinsically disordered proteins drive membrane curvature. *Nat Commun* **6**, 7875 (2015).
44. L. E. Olesen *et al.*, Solitary and Repetitive Binding Motifs for the AP2 Complex α-Appendage in Amphiphysin and Other Accessory Proteins*. *Journal of Biological Chemistry* **283**, 5099-5109 (2008).
45. B. Li *et al.*, Associations of genetic variants in endocytic trafficking of epidermal growth factor receptor super pathway with risk of nonsyndromic cleft lip with or without cleft palate. *Mol Genet Genomic Med* **6**, 1157-1167 (2018).
46. W. Li, R. Puertollano, J. S. Bonifacino, P. A. Overbeek, E. T. Everett, Disruption of the murine Ap2β1 gene causes nonsyndromic cleft palate. *Cleft Palate Craniofac J* **47**, 566-573 (2010).
47. I. Helbig *et al.*, A Recurrent Missense Variant in AP2M1 Impairs Clathrin-Mediated Endocytosis and Causes Developmental and Epileptic Encephalopathy. *Am J Hum Genet* **104**, 1060-1072 (2019).
48. C. M. Gorvin *et al.*, N-ethyl-N-nitrosourea-Induced Adaptor Protein 2 Sigma Subunit 1 (Ap2s1) Mutations Establish Ap2s1 Loss-of-Function Mice. *JBMR Plus* **1**, 3-15 (2017).
49. A. B. Arrigo, J. I. Lin, Endocytic Protein Defects in the Neural Crest Cell Lineage and Its Pathway Are Associated with Congenital Heart Defects. *Int J Mol Sci* **22** (2021).

50. S. Jung *et al.*, Disruption of adaptor protein 2μ (AP-2μ) in cochlear hair cells impairs vesicle reloading of synaptic release sites and hearing. *EMBO J* **34**, 2686-2702 (2015).
51. K. M. Dean *et al.*, Diagonally Scanned Light-Sheet Microscopy for Fast Volumetric Imaging of Adherent Cells. *Biophys J* **110**, 1456-1465 (2016).
52. S. Srinivasan *et al.*, A noncanonical role for dynamin-1 in regulating early stages of clathrin-mediated endocytosis in non-neuronal cells. *PLoS Biol* **16**, e2005377 (2018).
53. R. H. Kutner, X. Y. Zhang, J. Reiser, Production, concentration and titration of pseudotyped HIV-1-based lentiviral vectors. *Nature Protocols* **4**, 495-505 (2009).
54. S. D. Conner, S. L. Schmid, Differential requirements for AP-2 in clathrin-mediated endocytosis. *J Cell Biol* **162**, 773-779 (2003).
55. S. L. Schmid, E. Smythe, Stage-specific assays for coated pit formation and coated vesicle budding in vitro. *J Cell Biol* **114**, 869-880 (1991).
56. C. Yang *et al.*, Actin polymerization promotes invagination of flat clathrin-coated lattices in mammalian cells by pushing at lattice edges. *Nature Communications* **13**, 6127 (2022).
57. T. Svitkina, Imaging Cytoskeleton Components by Electron Microscopy. *Methods Mol Biol* **2364**, 25-52 (2022).
58. J. Jumper *et al.*, Highly accurate protein structure prediction with AlphaFold. *Nature* **596**, 583-589 (2021).
59. M. Varadi *et al.*, AlphaFold Protein Structure Database: massively expanding the structural coverage of protein-sequence space with high-accuracy models. *Nucleic Acids Research* **50**, D439-D444 (2021).

Figures and Tables

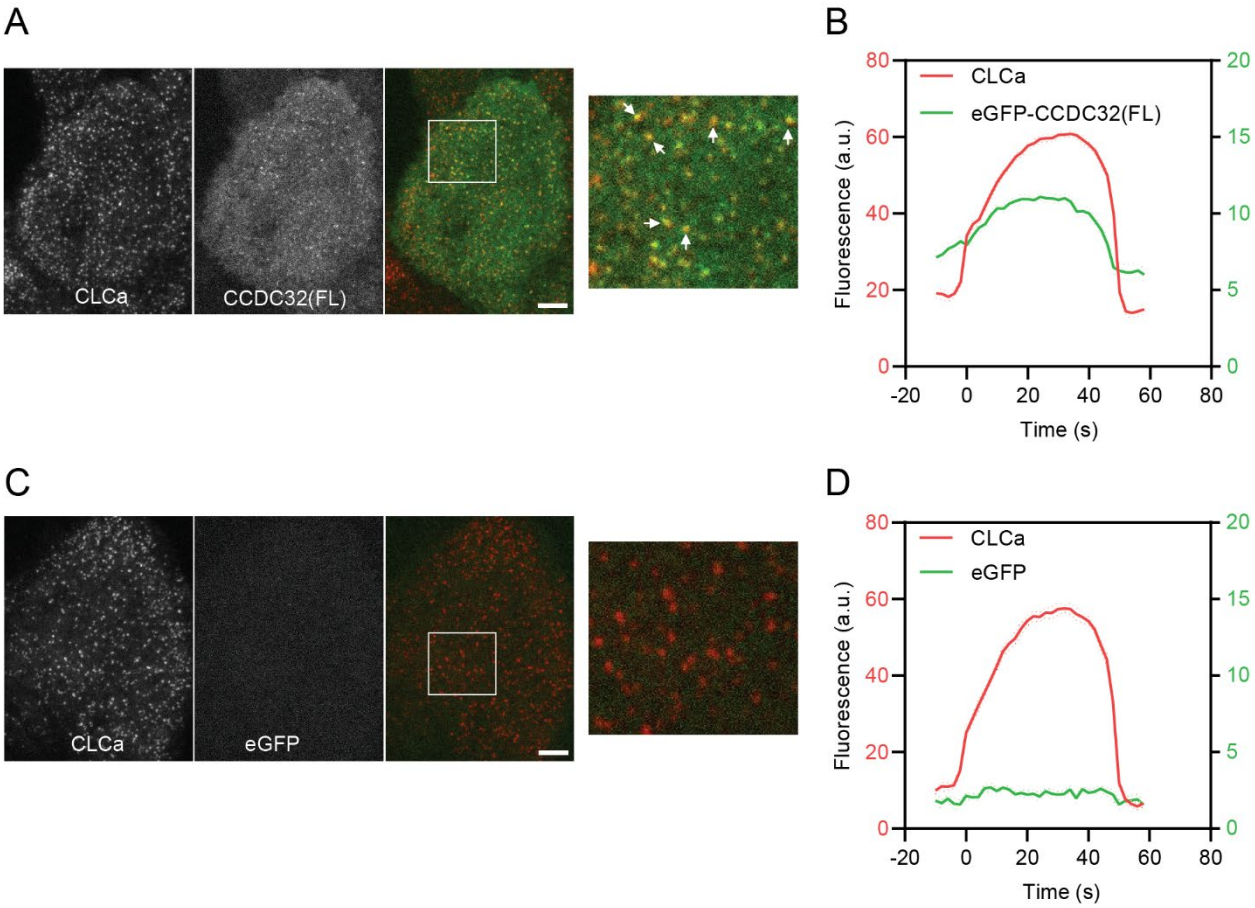

Figure 1: CCDC32 is recruited to clathrin-coated pits. (A) Representative TIRFM images of ARPE-HPV cells that stably express mRuby-CLCa and eGFP-CCDC32(FL). White arrows point to colocalized CLCa and CCDC32 clusters. White ROI is magnified on the right. Scale bar = 5μm. **(B)** Cohort-averaged fluorescence intensity traces of CCPs (marked with mRuby-CLCa) and CCP-enriched eGFP-CCDC32(FL). Number of tracks analyzed: 23699. **(C)** Representative TIRFM images of ARPE-HPV cells that stably express mRuby-CLCa and EGFP. White ROI is magnified on the right. Scale bar = 5μm. **(D)** Cohort-averaged fluorescence intensity traces of CCPs and CCP-enriched EGFP. Number of tracks analyzed: 46833.

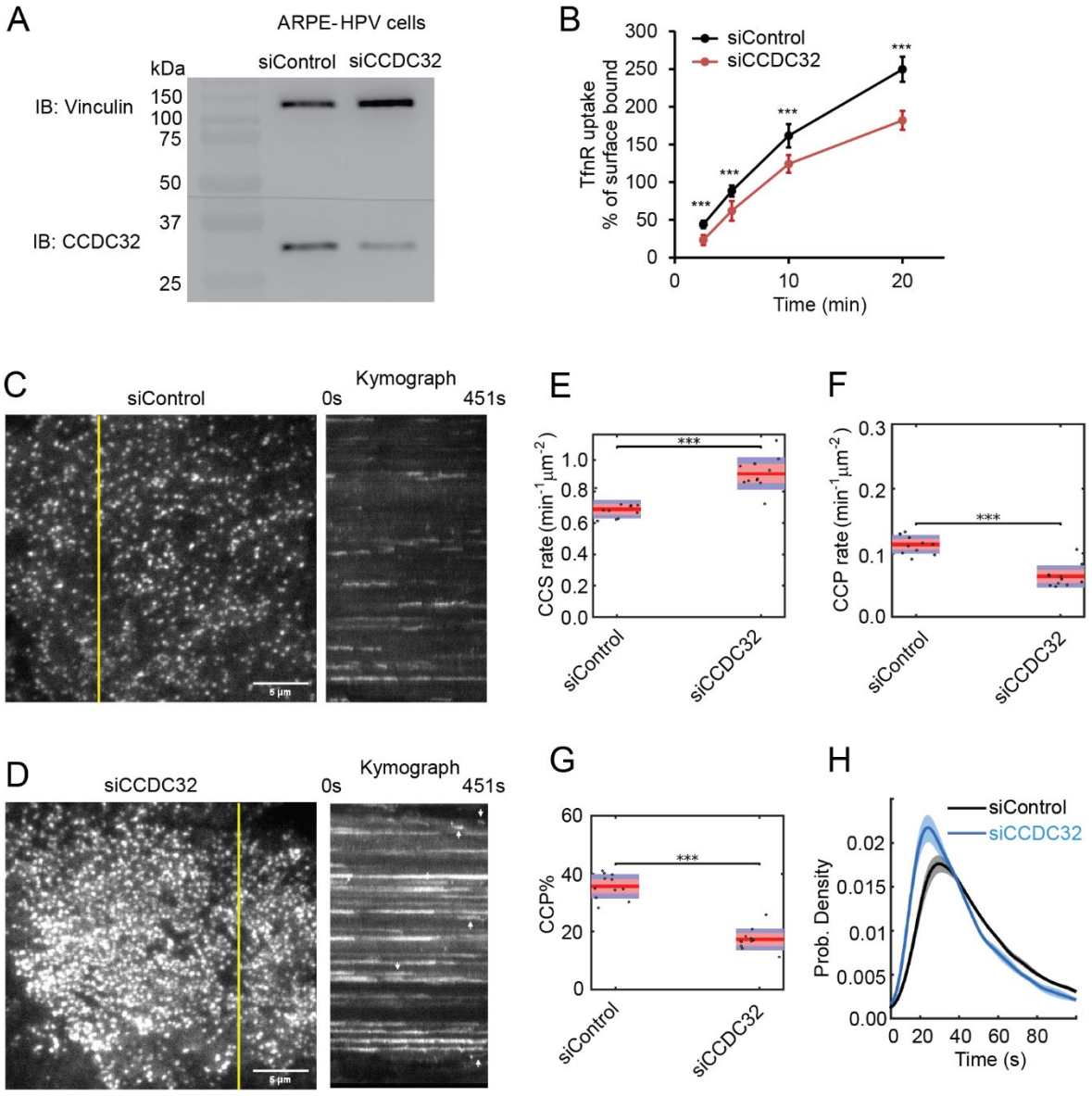

Figure 2: CCDC32 depletion inhibits Transferrin Receptor (TfnR) uptake and CCP maturation. **(A)** Immunoblotting (IB) shows efficient CCDC32 knockdown in ARPE-HPV cells by siRNA treatment. **(B)** Measurements of the uptake efficiency of TfnR. **(C-D)** Representative single frame images from TIRFM movies (7.5 min/movie, 1 frame/s, see Movies 1 and 2) and corresponding kymographs from region indicated by yellow lines of ARPE-HPV eGFP-CLCa cells treated with control siRNA (C) or CCDC32 siRNA (D). Scale bars = 5µm. **(E-G)** Effect of CCDC32 knockdown on the initiation rates of all CCSs (E) and *bona fide* CCPs (F), as well as the % of *bona fide* CCPs (G). Each dot represents a movie. Statistical analysis of the data in (E), (F) and (G) is the Wilcoxon rank sum test, ***, $p \leq 0.001$. **(H)** Lifetime distribution of *bona fide* CCPs. Data presented were obtained from a single experiment (n = 11 movies for each condition) that is representative of 3 independent repeats. Number of dynamic tracks analyzed: 143327 for siControl and 160513 for siCCDC32. Shadowed area indicates 95% confidential interval.

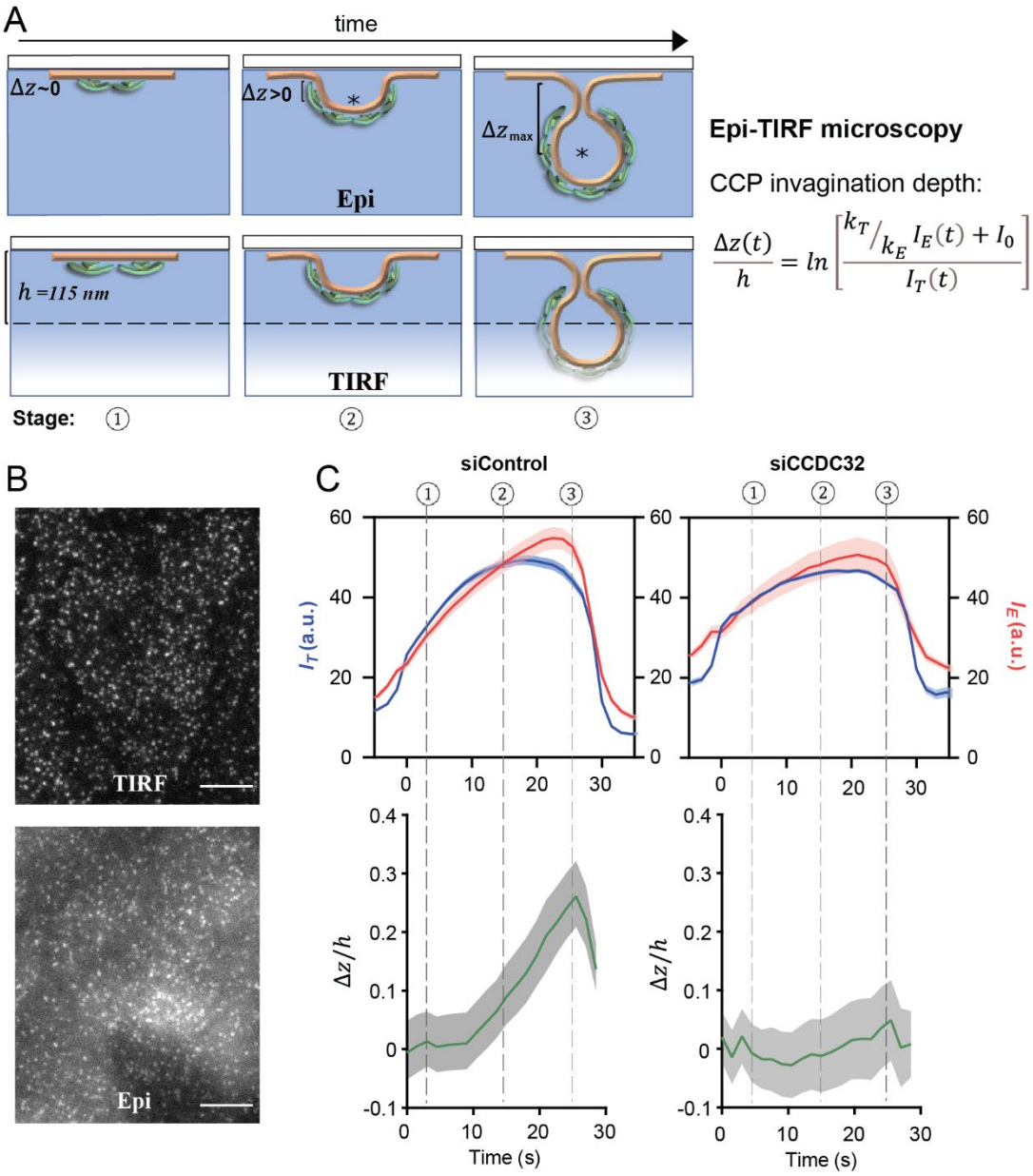

Figure 3: CCDC32 depletion inhibits CCP invagination. (A) Scheme of Epi-TIRF microscopy for measuring the invagination of CCPs using primary/subordinate tracking. $\Delta z(t)$ denotes the invagination depth of CCPs over time, while I_E and I_T denotes the cohort-averaged fluorescence intensity from Epi and TIRF channels, respectively. '*' indicates the mass center of clathrin coat. h=115nm is the evanescent depth of TIRF field, see more detail in ref.(15). **(B)** Representative Epi and TIRF microscopy images. Scale bars = 10μm. **(C)** Epi-TIRF microscopy analysis shows that knockdown CCDC32 strongly inhibited CCP invagination. Top: Cohort-averaged CCP fluorescence intensity traces from Epi and TIRF channels; bottom: calculated $\Delta z(t)/h$ curves. Data presented were obtained from n = 12 movies for each condition. Number of CCP tracks analyzed to obtain the $\Delta z/h$ curves: 5998 for siControl and 4418 for siCCDC32. Shadowed area indicates 95% confidential interval.

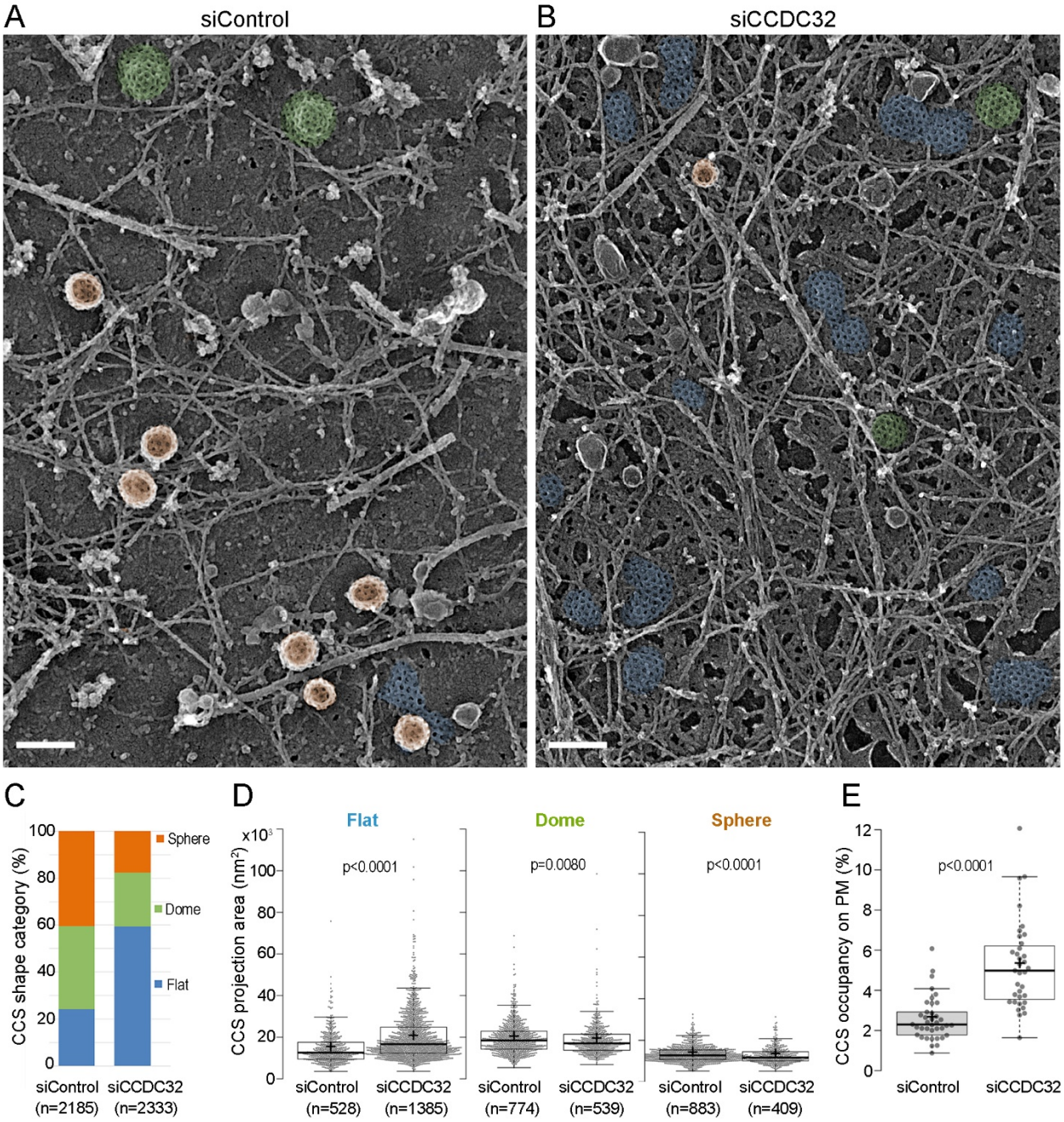

Figure 4: Flat clathrin lattices accumulate in cells depleted of CCDC32. (A-B) Representative PREM images of ARPE19 cells treated with control siRNA (A) or CCDC32 siRNA (B) showing flat (blue), dome-shaped (green) and spherical (orange) CCSs. Scale bars = 200nm. **(C-E)** Quantification of the clathrin-coated structure (CCS) shape category (C), the CCS projection area (D), and the CCS occupancy on the plasma membrane (PM) (E). Each dot in (E) represents an individual fragment of the PM; the number of cell membrane fragments analyzed is 38 for siControl cells and 35 for siCCDC32 cells from two independent experiments, n = number of CCS. Statistical tests were performed using Mann-Whiney test (D) or unpaired t-test (E).

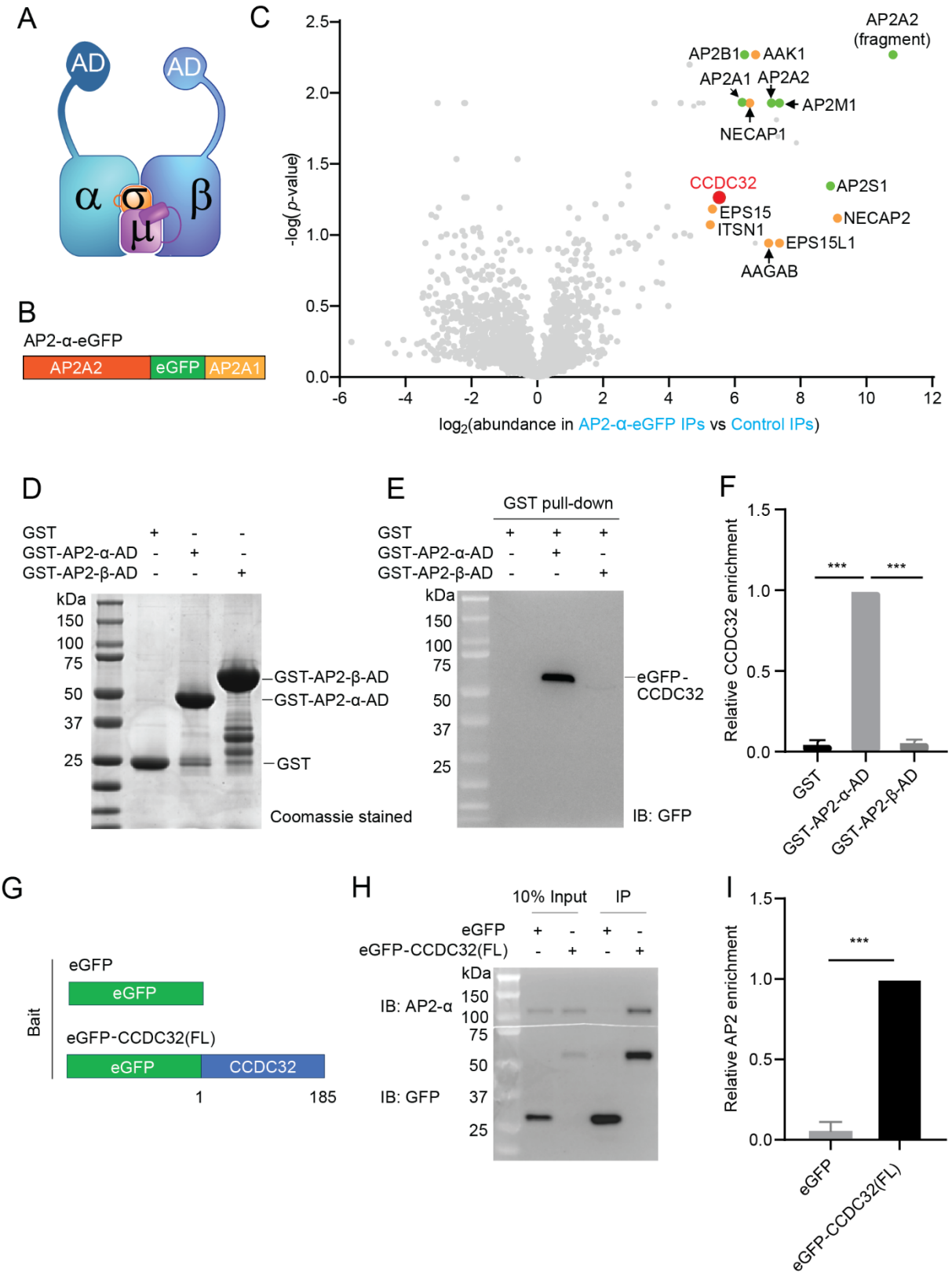
A
AD
AD
α
σ
μ
β
B
AP2-α-eGFP
AP2A2
eGFP
AP2A1
C
-log(p-value)
log2(abundance in AP2-α-eGFP IPs vs Control IPs)
AP2A2 (fragment)
AP2B1
AAK1
AP2A1
AP2A2
AP2M1
NECAP1
CCDC32
AP2S1
EPS15
NECAP2
ITSN1
EPS15L1
AAGAB
D
GST
GST-AP2-α-AD
GST-AP2-β-AD
kDa
150
100
75
50
37
25
GST-AP2-β-AD
GST-AP2-α-AD
GST
Coomassie stained
E
GST pull-down
GST
GST-AP2-α-AD
GST-AP2-β-AD
kDa
eGFP-CCDC32
IB: GFP
F
Relative CCDC32 enrichment
***
***
GST
GST-AP2-α-AD
GST-AP2-β-AD
G
Bait
eGFP
eGFP
eGFP-CCDC32(FL)
eGFP
CCDC32
1
185
H
10% Input
IP
eGFP
eGFP-CCDC32(FL)
kDa
IB: AP2-α
IB: GFP
I
Relative AP2 enrichment
***
eGFP
eGFP-CCDC32(FL)

Figure 5: CCDC32 interacts with AP2 through the α appendage domain. (A) AP2 structure. AD: appendage domain. **(B-C)** Immunoprecipitation (IP) of eGFP from naive ARPE-HPV cells (control IPs) or ARPE-HPV cells that stably express AP2-α-eGFP (AP2-α-eGFP IPs) using anti-GFP beads. (B) The domain structure of AP2-α-eGFP. (C) Volcano plot after mass spectrometry analysis of the IP samples for protein ID and abundance detection. Green: AP2 subunits; orange: known AP2 interactors. **(D-F)** GST pull-down assays. (D) Coomassie blue stained SDS-page gel of purified GST, GST-AP2-α-AD, and GST-AP2-β-AD. (E) Representative western blot result of n=3 GST pull-down assay from ARPE-HPV eGFP-CCDC32(FL) cell lysate using purified GST, GST-AP2-α-AD, or GST-AP2-β-AD. The amount of bait GST-proteins is shown in (D), and the pulled down eGFP-CCDC32 was detected by immunoblotting (IB) of GFP. (F) Relative CCDC32 enrichments quantified from immunoblotting results as shown in (E). **(G-I)** IP of eGFP from ARPE-HPV cells that stably express eGFP or eGFP-CCDC32(FL) using anti-GFP magnetic beads. (G) The domain structures of eGFP and eGFP-CCDC32(FL). (H) Representative immunoblotting result of n=3 IP samples. (I) Relative AP2 enrichments quantified from immunoblotting results. Error bars are SD. Two-tailed student's t-test: ***, $p \leqslant 0.001$.

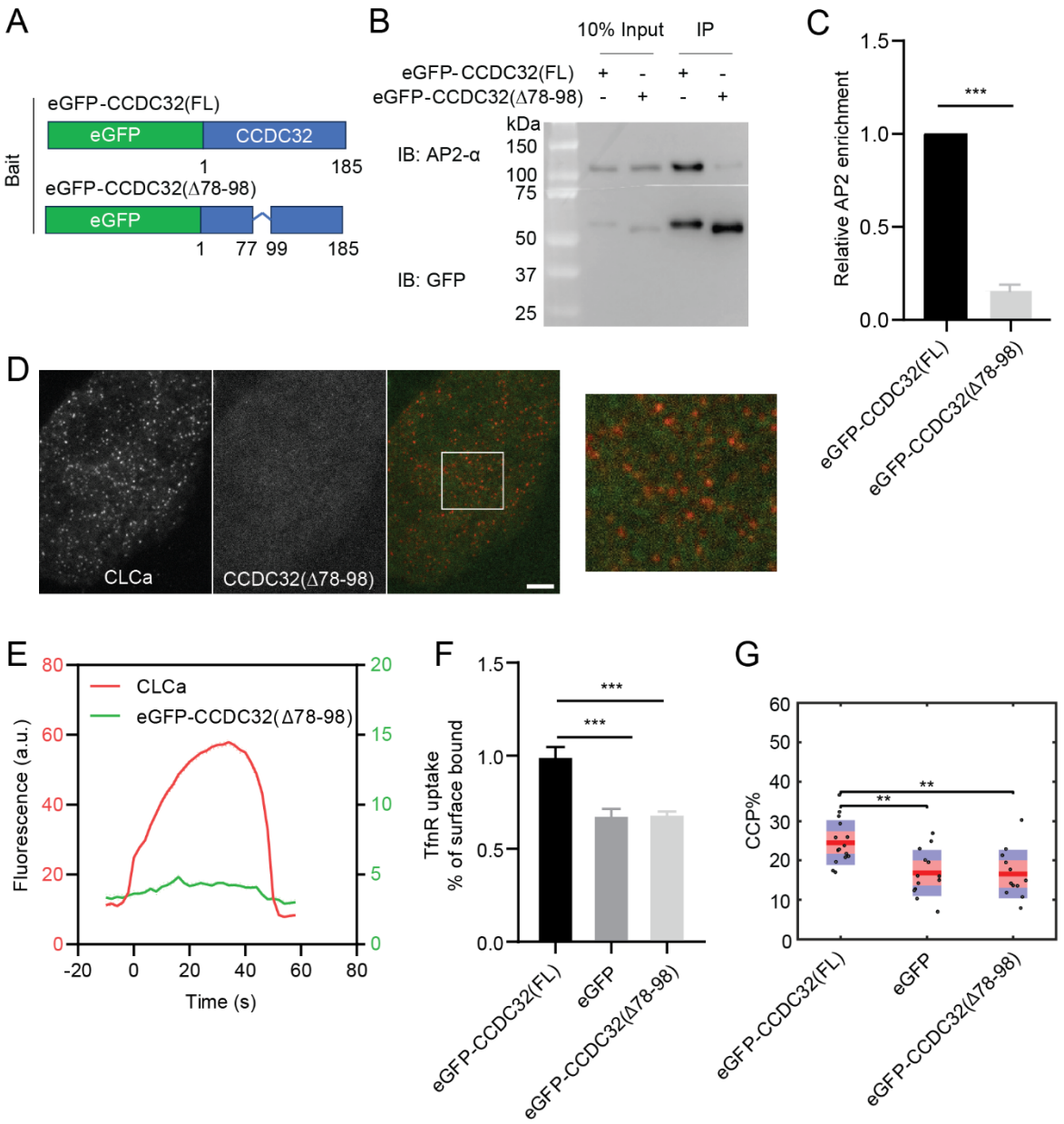

Figure 6: The coiled-coil domain of CCDC32 mediates CCDC32-AP2 interactions. (A-C) IP of eGFP from ARPE-HPV cells that stably express eGFP-CCDC32(FL) or eGFP-CCDC32(Δ78-98) using anti-GFP beads. (A) The domain structures of eGFP-CCDC32(WT) and eGFP-CCDC32(Δ78-98). (B) Representative Immunoblotting result of n=3 IP samples. (C) Relative AP2 enrichments that were quantified from (B). (**D**) Representative TIRFM images of ARPE-HPV cells that stably express mRuby-CLCa and eGFP-CCDC32(Δ78-98). White ROI is magnified on the right. Scale bar = 5μm. (**E**) Cohort-averaged fluorescence intensity traces of CCPs and CCP-enriched eGFP-CCDC32(Δ78-98). Number of tracks analyzed: 37892. **(F-G)** TfnR uptake efficiency (F) and CCP% (G) of ARPE-HPV cells that stably express eGFP-CCDC32(WT), eGFP, or eGFP-CCDC32(Δ78-98), and with siRNA-mediated knockdown of endogenous CCDC32. Each dot represents a movie. Statistical analysis of the data in (F) is two-tailed student's t-test: ***, $p \leq 0.001$. Statistical analysis of the data in (G) is the Wilcoxon rank sum test, **, $p \leq 0.01$.

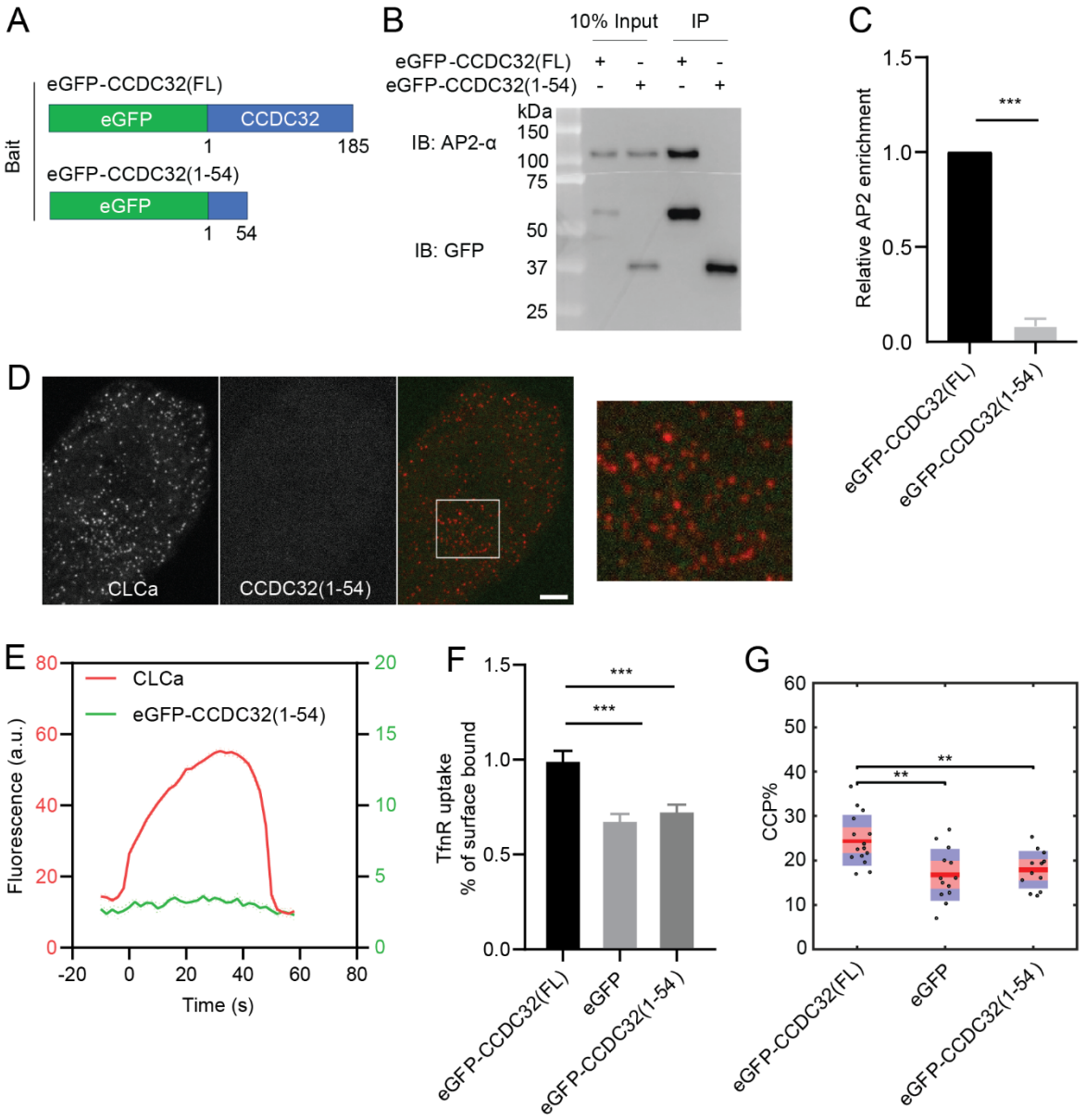

Figure 7: Disease-causing nonsense mutation in CCDC32 loses AP2 interaction capacity and inhibits CME. (A-C) IP of eGFP from ARPE-HPV cells that stably express eGFP-CCDC32(FL) or eGFP-CCDC32(1-54) using anti-GFP magnetic beads. (A) The domain structures of eGFP-CCDC32(FL) and eGFP-CCDC32(1-54). (B) Representative immunoblotting result of n=3 IP samples. (C) Relative AP2 enrichments quantified from immunoblotting results. **(D)** Representative TIRFM images of ARPE-HPV cells that stably express mRuby-CLCa and eGFP-CCDC32(1-54). White ROI is magnified on the right. Scale bar = 5μm. **(E)** Cohort-averaged fluorescence intensity traces of CCPs and CCP-enriched eGFP-CCDC32(1-54). Number of tracks analyzed: 28658. **(F-G)** TfnR uptake efficiency (F) and CCP% (G) of ARPE-HPV cells that stably express eGFP-CCDC32(FL), eGFP, or eGFP-CCDC32(1-54), and with siRNA-mediated knockdown of endogenous CCDC32. Statistical analysis of the data in (F) is two-tailed student's t-test: ***, $p \leq 0.001$. Statistical analysis of the data in (G) is the Wilcoxon rank sum test, **, $p \leq 0.01$.

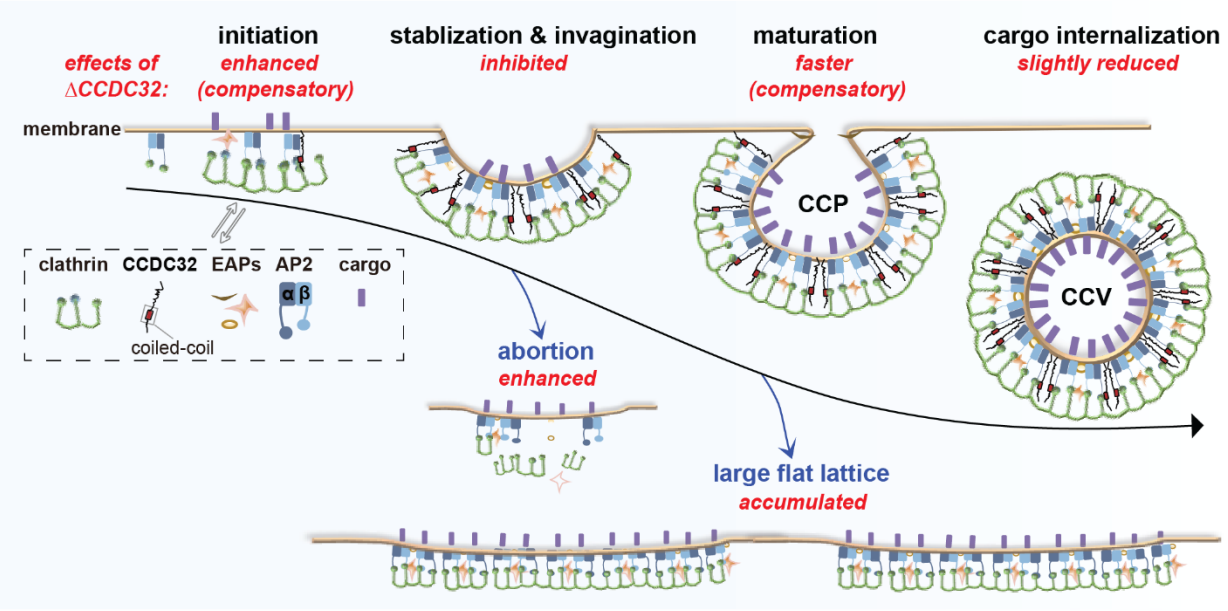

Figure 8: Cartoon illustration of CCDC32-AP2 interactions that regulate CME. The coiled-coil domain of CCDC32 and the α-AD of AP2 are essential for CCDC32-AP2 interactions. Depleting CCDC32 (ΔCCDC32) inhibits CCP stabilization and invagination, resulting in enhanced CCS abortion and accumulated flat clathrin lattices. As a compensation effect, CCS initiation is enhanced and CCP maturation is faster, resulting in only slightly reduced cargo internalization. EAPs: endocytic accessory proteins.

Movie 1: Time-lapse TIRFM imaging of ARPE-HPV eGFP-CLCa cells that were treated with control siRNA. Images were obtained at 1 frame/s and collected for 7.5 min. Movie is accelerated 25-fold.

Movie 2: Time-lapse TIRFM imaging of ARPE-HPV eGFP-CLCa cells that were treated with CCDC32 siRNA. Images were obtained at 1 frame/s and collected for 7.5 min. Movie is accelerated 25-fold.

Supplementary Figures:

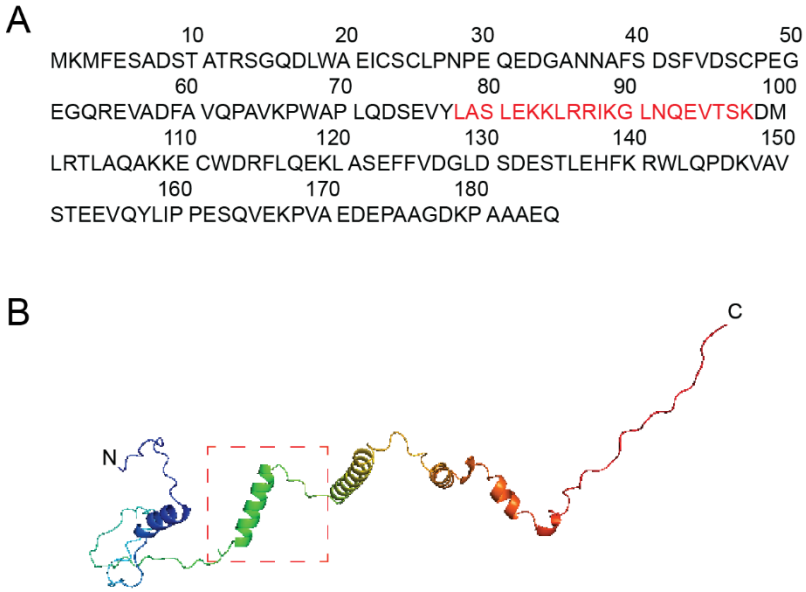

Figure S1: The sequence and structure of CCDC32. (**A**) Amino acid sequence of CCDC32. Red font: coiled-coil domain. (**B**) The structure of CCDC32 predicted by AlphaFold2 (58, 59). Dashed box indicates aa78-98.

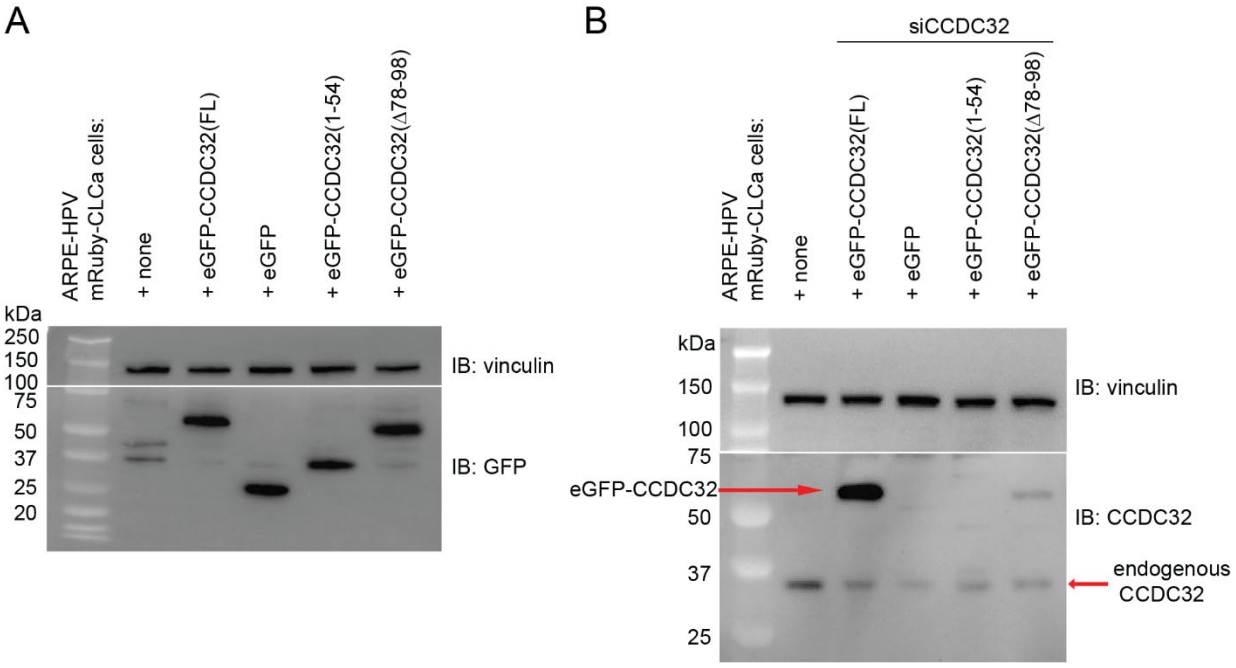

Figure S2: (A) Western blotting indicates similar expression levels of exogenous eGFP-CCDC32(FL), eGFP, eGFP-CCDC32(1-54) and eGFP-CCDC32(Δ78-98) in ARPE-HPV mRuby-CLCa cells. Note that the anti-CCDC32 antibody does not detect the truncated mutants as well

as full-length; **(B)** siCCDC32 knocked down endogenous CCDC32 but not exogenously introduced eGFP-CCDC32 from ARPE-HPV mRuby-CLCa cells.

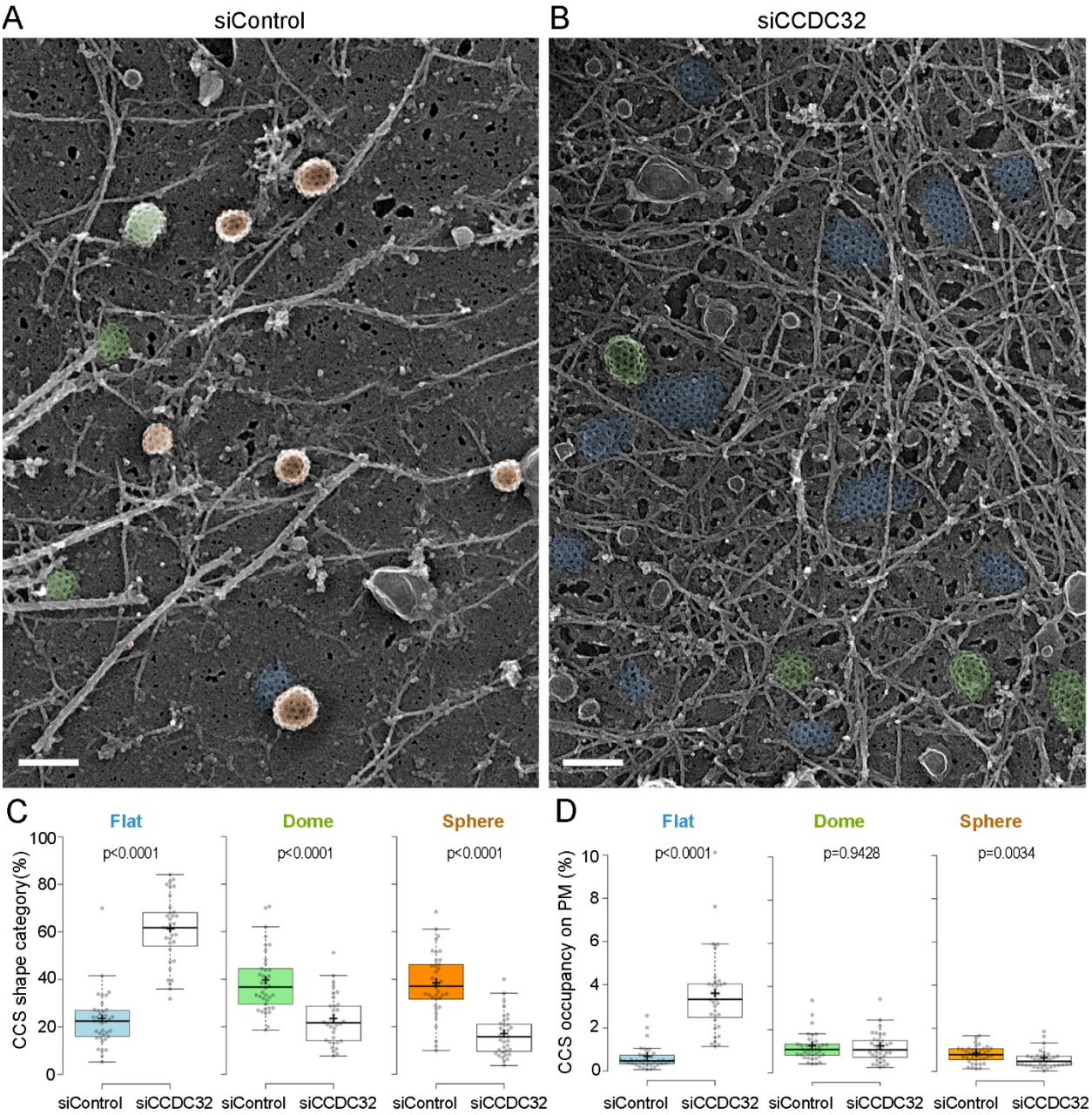

Figure S3: CCDC32 knockdown shifts the shapes of clathrin-coated structures. (A-B) Representative PREM images of ARPE-HPV cells treated with control siRNA (A) or CCDC32 siRNA (B). Scale bars = 200 nm. **(C-D)** Quantification of the CCS shape category (C) and CCS occupancy on PM (D). Each dot represents an individual fragment of the plasma membrane; the number of plasma membrane fragments analyzed is 38 for siControl and 35 for siCCDC32 from two independent experiments. Statistical tests were performed using either unpaired t-test or Mann-Whiney test depending on normality of distributed values.

	Abundance					
	Control IPs			AP2-α-eGFP IPs		
Gene	**#1**	**#2**	**#3**	**#4**	**#5**	**#6**
AP2A1	2.E+06	1.E+06	6.E+05	1.E+08	1.E+08	2.E+08
AP2A2	4.E+06	1.E+06	7.E+05	3.E+08	3.E+08	3.E+08
AP2B1	7.E+06	6.E+06	3.E+06	7.E+08	6.E+08	6.E+08
AP2M1	1.E+06	8.E+05	2.E+05	2.E+08	1.E+08	2.E+08
AP2S1	1.E+05	5.E+04	9.E+03	2.E+07	2.E+07	5.E+07
CCDC32	**0.E+00**	**0.E+00**	**0.E+00**	**3.E+06**	**2.E+06**	**2.E+06**
AAK1	7.E+04	1.E+05	3.E+04	2.E+07	1.E+07	2.E+07
EPS15	2.E+06	3.E+05	2.E+05	3.E+07	3.E+07	3.E+07
EPS15L	3.E+05	1.E+04	2.E+04	1.E+07	1.E+07	1.E+07
FCHO2	4.E+04	3.E+04	2.E+04	1.E+06	1.E+06	1.E+06
ITSN1	1.E+04	0.E+00	0.E+00	1.E+06	9.E+05	7.E+05
NECAP1	9.E+04	8.E+04	3.E+04	9.E+06	7.E+06	1.E+07
NECAP2	1.E+05	7.E+03	1.E+04	2.E+07	2.E+07	2.E+07
AAGAB	9.E+00	0.E+00	0.E+00	3.E+06	4.E+06	7.E+06

Table S1: ID and abundances of key proteins detected in IP samples by Mass Spectroscopy analysis. #1-#3: 3 independent repeats of control IPs; #4-#6: 3 independent repeats of AP2-α-eGFP IPs.